

# Metal–Insulator Transition via Ion Irradiation in Epitaxial $\text{La}_{0.7}\text{Sr}_{0.3}\text{MnO}_{3-\delta}$ Thin Films

Lei Cao,\* Andreas Herklotz, Diana Rata, Chenyang Yin, Oleg Petravic, Ulrich Kentsch, Manfred Helm, and Shengqiang Zhou

Complex oxides provide rich physics related to ionic defects. For the proper tuning of functionalities in oxide heterostructures, it is highly desired to develop fast, effective, and low-temperature routes for the dynamic modification of defect concentration and distribution. Herein, the use of helium implantation to efficiently control the vacancy profiles in epitaxial  $\text{La}_{0.7}\text{Sr}_{0.3}\text{MnO}_{3-\delta}$  thin films is reported. The viability of this approach is supported by lattice expansion in the out-of-plane lattice direction and dramatic change in physical properties, i.e., a transition from ferromagnetic metallic to antiferromagnetic insulating. In particular, a significant increase of resistivity up to four orders of magnitude is evidenced at room temperature, upon implantation of highly energetic He ions. The result offers an attractive means for tuning the emergent physical properties of oxide thin films via strong coupling between strain, defects, and valence.

and electrocatalysis.<sup>[1–3]</sup> The concentration and distribution of point defects—primarily the oxygen vacancies—strongly affect the valence states of transition metals, charge carrier populations, and spin configurations, which are essential for improving or even accessing new properties in perovskite oxides.<sup>[4–6]</sup> Such an extraordinary dependence of functionalities on anion stoichiometry enables defect engineering as a new path to design next-generation oxide-based electronic/spintronic devices.<sup>[7–10]</sup> In addition, the presence of oxygen vacancies is known to induce an expansion of the perovskite lattice in recent studies.<sup>[11–13]</sup> The dynamic control of oxygen deficiency, which has been proven by several methods (e.g., top-

## 1. Introduction

The manipulation of strong electronic correlations in complex oxides has attracted a great deal of interest at the forefront of solid-state physics research, with particular emphasis on emergent phenomena and novel functionalities such as superconductivity, colossal magnetoresistance, multiferroics,

otactic reduction, ionic liquid gating, oxygen getter), can thus act as an alternative way to alter the crystal lattice in addition to standard heteroepitaxy.<sup>[14–16]</sup> However, in the aspect of ion irradiation, only a few systematic studies have been conducted to elucidate the fundamental link between strain state and oxygen defects.<sup>[12]</sup> As a result, the full details of vacancy-induced lattice strain and its impact on electronic properties remain unknown.


Among the promising candidates suited for device application, the manganite,  $\text{La}_{0.7}\text{Sr}_{0.3}\text{MnO}_{3-\delta}$  (LSMO) has attracted significant attention due to its high Curie temperature and half-metallic behavior well above room temperature.<sup>[17,18]</sup> Previous studies have shown a strong lattice–charge–spin–orbital coupling in LSMO series due to the highly correlated electrons.<sup>[19,20]</sup> Therefore, epitaxial LSMO thin films were selected as a platform to validate the effects of vacancy modification on the lattice structure and physical properties.

In this work, we report on an effective modification of defect in-depth profiles in epitaxial LSMO thin films using helium implantation. By tailoring the incident energy and fluence of the He-ion beam, the vacancy concentration and distribution are actively tuned throughout the entire film. As confirmed by X-ray diffraction techniques, the generation of defects induces a uniaxial lattice expansion solely in the out-of-plane direction without any relaxation of the in-plane lattice constant, which completely changes the strain type of the film (i.e., from tensile strain to compressive strain). This allows for a tunable modification in both the magnetic and electrical transport properties. In particular, the metal–insulator transition, manifesting itself as an increase of resistivity up to four orders of magnitude, has been observed at higher irradiation fluence. Thus, this study opens a

L. Cao, U. Kentsch, M. Helm, S. Zhou  
Institute of Ion Beam Physics and Materials Research  
Helmholtz-Zentrum Dresden-Rossendorf  
Dresden 01328, Germany  
E-mail: l.cao@hzdr.de

A. Herklotz, D. Rata  
Institute of Physics  
Martin Luther University Halle-Wittenberg  
Halle 06120, Germany

C. Yin, O. Petravic  
Jülich Centre for Neutron Science (JCNS-2) and Peter Grünberg Institut (PGI-4)  
JARA-FIT  
Forschungszentrum Jülich GmbH  
Jülich 52425, Germany

 The ORCID identification number(s) for the author(s) of this article can be found under <https://doi.org/10.1002/pssr.202100278>.

© 2021 The Authors. physica status solidi (RRL) Rapid Research Letters published by Wiley-VCH GmbH. This is an open access article under the terms of the Creative Commons Attribution-NonCommercial-NoDerivs License, which permits use and distribution in any medium, provided the original work is properly cited, the use is non-commercial and no modifications or adaptations are made.

DOI: 10.1002/pssr.202100278

new path for the fine depth-dependent tuning of the material properties in oxides.

## 2. Results and Discussion

LSMO films of 50 nm thickness were deposited on (001) SrTiO<sub>3</sub> (STO) single-crystalline substrates by high-oxygen-pressure sputter deposition (HOPSD), with the optimal growth parameters shown in the Experimental Section. Note that LSMO has a rhombohedral structure ( $a = b = 5.4967 \text{ \AA}$ ,  $c = 13.3321 \text{ \AA}$ ), which can be represented as pseudocubic with lattice constants of  $a = b = c = 3.8741 \text{ \AA}$ .<sup>[7,21]</sup> Due to the small lattice mismatch, the LSMO thin films are grown coherently strained on SrTiO<sub>3</sub> ( $a = 3.905 \text{ \AA}$ ) substrate. After deposition, the films were implanted with He-ion beams at various energies to achieve different defect distributions. For the implantation at 3.5 keV, the incident He ions stop within the film. Two different fluences were adopted to generate different defect concentrations. When the implantation energy is increased to 50 keV, the He-ion beam penetrates deeper into the substrate.

Figure 1a,b displays the  $\omega$ -2 $\theta$  X-ray diffraction (XRD) patterns of the LSMO films. For the pristine state, the film exhibits well-defined (001) and (002) Bragg peaks at higher two-theta values than the substrate peak, in agreement with the expected out-of-plane lattice constant for a perovskite phase. Laue fringes further indicate sharp interfaces and flat surfaces. After He-ion implantations at an energy of 3.5 keV and a fluence of  $1 \times 10^{15} \text{ cm}^{-2}$ , a shift of the LSMO peaks toward lower angles is observed, which indicates an elongated out-of-plane lattice constant. This lattice expansion is usually considered an indication of oxygen deficiency in LSMO films, as the Mn<sup>4+</sup> valence state changes to Mn<sup>3+</sup>, which has a larger ionic radius.<sup>[7,22]</sup> In the detailed XRD scan around the (002) Bragg peak, a notable broadening of the film peak is also observed, which is caused by the Gaussian-like distribution profile of implanted He ions. Upon increasing the He fluence to  $5 \times 10^{15} \text{ cm}^{-2}$ , this effect becomes more evident as the (002)-LSMO reflection further splits into two broad peaks. To better evaluate the defect concentration and

distribution at various implantation conditions, Stopping and Range of Ions in Matter (SRIM) simulations were performed. According to the simulation results in Figure 1c, more than half the amount of total displacement per atom (DPA) induced by He ions arises from oxygen vacancies in the SRIM simulation. In particular, the beam penetrates deeply into the substrate when highly energetic He ions with 50 keV are utilized for the implantation. This creates a relatively flat defect profile in the film region. As a result, a single peak at  $45.7^\circ$  is observed from the modified LSMO film, indicating a uniform vacancy distribution throughout the entire film. Here we note that the fluence of the 50 keV He-ion beam is increased to  $5 \times 10^{16}$  and  $2.5 \times 10^{16} \text{ cm}^{-2}$ , respectively, to achieve a comparative defect concentration with the implantation at 3.5 keV. In addition, a significant swelling due to He implantation is also expected in the buried SrTiO<sub>3</sub> substrate region up to 400 nm, which results in the broad peak observed at about  $44^\circ$ .<sup>[23–25]</sup> Our results show consistent observation with the measured and simulated XRD spectra for the pure STO substrate irradiated at comparable energy and fluence.

In addition to the elongation of the out-of-plane lattice parameter, the strain change after He implantation is monitored by reciprocal space mapping. Figure 2 compares the corresponding strain states for the samples implanted at various conditions. The diffraction spots of all the LSMO films locate at the same  $q_x$  positions as the SrTiO<sub>3</sub> substrate, whereas a shift in  $q_z$  is clearly visible. This indicates that the in-plane lattice parameters of LSMO films remain identical to that of the substrate without any lattice relaxations after He implantation. The variations of the  $q_z$  value correspond well to the observation from  $\omega$ -2 $\theta$  XRD scans, which corroborates the sole expansion of the lattice in the out-of-plane direction. It is also noteworthy that the He implantation did not trigger a topotactic transition, which was previously reported by hydrogen plasma and postannealing treatment.<sup>[7,26]</sup> As a kinetic process at high energy, the bombardment with He ions results in a wide distribution of Frenkel pairs (i.e., point defects). On the other hand, as helium is a noble gas and does not form any chemical bond with the host matrix, it is the formation of point defects that induces the structural modification. Moreover, two different

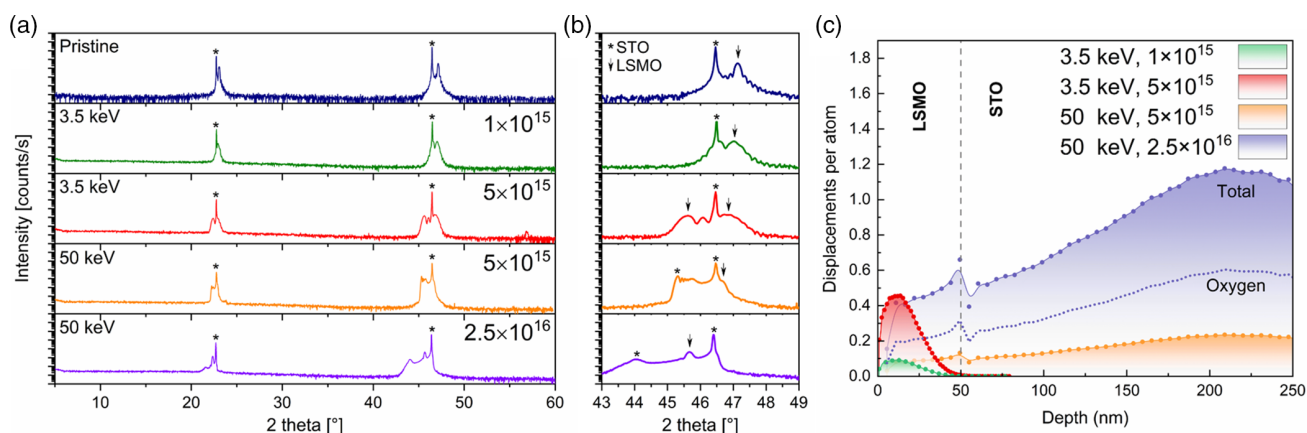


**Figure 1.** a,b) XRD  $\omega$ -2 $\theta$  patterns of epitaxial LSMO thin films on a SrTiO<sub>3</sub> (001) substrate implanted by He-ion beams with various incident energies (3.5 and 50 keV) and fluence ranging from  $1 \times 10^{15}$  to  $2.5 \times 10^{16} \text{ cm}^{-2}$ , respectively. The peaks labeled with stars are from SrTiO<sub>3</sub>, while those labeled with arrows are from LSMO. c) SRIM simulation results of displacement per atom (DPA) at various implantation parameters. In particular, the DPA profile of an oxygen atom is denoted by the dashed line for the sample implanted at 50 keV with the fluence of  $2.5 \times 10^{16} \text{ cm}^{-2}$ .

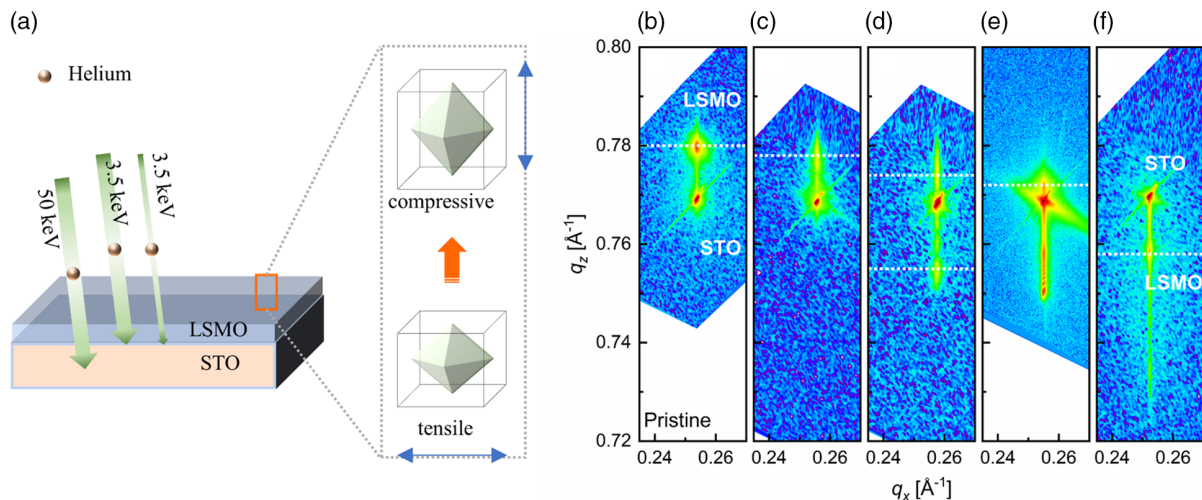


**Figure 2.** a) Schematic of helium implantation into LSMO films and corresponding strain modification from tensile to compressive. b–f) Reciprocal space maps around the (103) peaks of the LSMO thin film implanted by He-ion beams: b) pristine state; c) 3.5 keV He ions with fluence of  $1 \times 10^{15} \text{ cm}^{-2}$ ; d) 3.5 keV He ions with fluence of  $5 \times 10^{15} \text{ cm}^{-2}$ ; e) 50 keV He ions with fluence of  $5 \times 10^{15} \text{ cm}^{-2}$ ; f) 50 keV He ions with fluence of  $2.5 \times 10^{16} \text{ cm}^{-2}$ . The positions for film peaks are denoted by the white dashed lines.

energies were used for the study, i.e., 3.5 and 50 keV. In the case of 50 keV, helium ions mainly stay in the STO substrate. However, the irradiation leads to similar structure modification for the LSMO film. This also rules out the role of the He ions inserted.

To confirm that the high fluence and energies used in this study are still below the threshold for amorphization, both random and channeling Rutherford backscattering spectrometry (RBS) spectra were measured for the as-prepared and implanted films. As shown in Figure 3a, the as-prepared LSMO film exhibits a large difference in the yield between the random and channeling spectra, which indicates a good crystallinity. With increasing fluence of incident He ions, more damage to the crystal lattice upon ion bombardment occurs, and an enhanced yield in the channeling spectra is observed. In detail, the RBS yields for La and Mn reveal significant increase at the depth close to the surface after implantation at 3.5 keV, which correlates well with the results of the DPA profile. In contrast, a channeling effect is

still well preserved for the sample with the highest number of defects (implanted at 50 keV with a fluence of  $2.5 \times 10^{16} \text{ cm}^{-2}$ ). Thus, for this fluence, we conclude that the LSMO film is still crystalline, as expected.

XRR measurements were further conducted to determine the corresponding change of roughness at both the surface and film/substrate interface. As shown in Figure 3b, all the films exhibit long-lived Kiessig fringes, which indicates a relatively small change of roughness after implantation. At an incident energy of 3.5 keV, the implantation depth is below the thickness of the film, and no perturbations are induced at the film/substrate interface. Only the surface roughness is found to increase with the incident fluence of He ions, as shown in Figure 3c. For the sample implanted at 50 keV, the He ions are implanted deeper into the substrate, and an increase of interface roughness is evident. Nevertheless, the roughness for both implanted cases is still less than 3.5 nm, which confirms a uniform film and smooth surfaces.

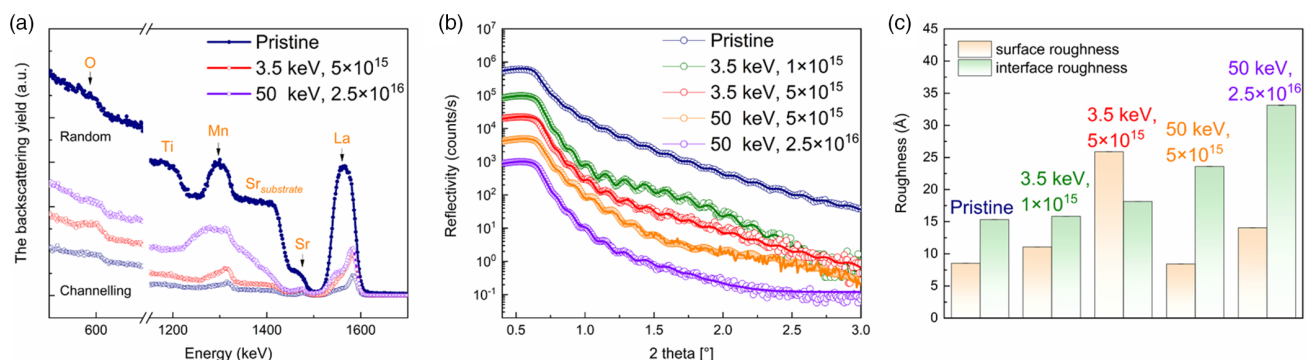


**Figure 3.** a) RBS random and channeling spectra obtained from samples implanted with He ions at various conditions. b) The experimental (open circles) and simulated (solid curves) X-ray reflectivities (XRRs) for LSMO films implanted with He ions at various conditions. For clarity, the data are equally shifted. c) The surface and interface roughness obtained from the fitting of the obtained XRR data.

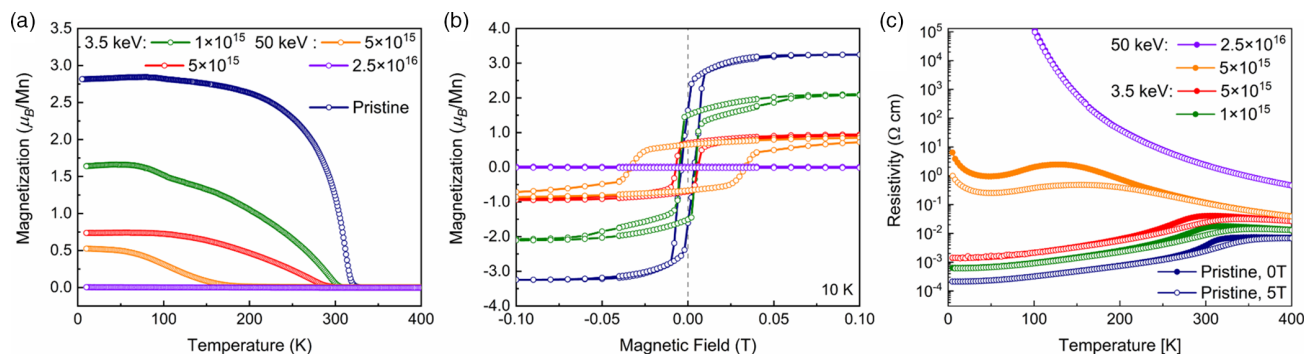


**Figure 4.** a) Temperature-dependent magnetization of the pristine and implanted LSMO thin film samples, measured at 100 Oe. b) Hysteresis loops measured at 10 K with the magnetic field applied in-plane for various implanted states. c) Temperature-dependent resistivity measured for various implanted states at zero field (solid symbols) and a magnetic field of 5 T (open symbols).

Attributed to the complex nature of exchange interactions in transition metal oxides, small changes to oxygen vacancy concentration and distribution can lead to strong modifications of electronic and magnetic properties.<sup>[27–29]</sup>

**Figure 4a** plots the temperature-dependent magnetization for all the films measured after field cooling. The pristine state exhibits ferromagnetic behavior with a high Curie temperature above 300 K. The result is in good agreement with the domination of the double-exchange mechanism among the *d*-orbital magnetic ions ( $\text{Mn}^{3+}$  and  $\text{Mn}^{4+}$ ) for this stoichiometry.<sup>[30–32]</sup> After implantation, we expect that the nominal manganese valence is reduced due to the introduction of defects (primarily oxygen vacancies), in which the fraction of  $\text{Mn}^{3+}$  ions becomes more abundant. As a result, a  $\text{Mn}^{3+}\text{--O--Mn}^{3+}$  combination is prevalent among most manganese centers in the system and a strong superexchange coupling starts to take over. Thus, a suppression of Curie temperature is observed with increasing He doses in the field cooling curves. Strikingly, at a high fluence of  $2.5 \times 10^{16} \text{ cm}^{-2}$  at 50 keV, the implanted LSMO films exhibit hardly any magnetization and the magnetization-field loop measured at 10 K (Figure 4b) does not show any discernible hysteresis. The suppression of macroscopic magnetization could be attributed to the emergence of local antiferromagnetic interactions or long-range order of antiferromagnetism. In addition, a significant enhancement of the coercive field is observed for the sample implanted with  $5 \times 10^{15} \text{ cm}^{-2}$  at 50 keV, which could be favourable for applications.

On the other hand, the change in magnetic behaviour is accompanied by a significant modification of electrical transport properties in the LSMO system. As shown in Figure 4c, the as-prepared state exhibits metallic behavior. With increasing defect concentration, a clear increase of resistivity is observed. At lower beam energy, the effect of He implantation is inhomogeneous along the depth. The resistivity data are mainly governed by the layer with low He concentration close to the STO substrate interface that exhibits higher conductance. Therefore, the low-energy samples are still metallic (red curve). It is worth noting that the enhancement in resistivity is accompanied by a shift of maximum value toward lower temperature, which shows good agreement with the observed suppression of the Curie temperature. At a higher beam energy of 50 keV, a metal-to-insulator transition occurs, where a relatively homogeneous DPA profile

is achieved throughout the entire film. In particular, the resistivity increases four orders of magnitude even at room temperature with the fluence of  $2.5 \times 10^{16} \text{ cm}^{-2}$ . Together with the XRD pattern measured for this sample, the observed magnetic and electrical properties resemble well the homogeneous oxygen-deficient state achieved by vacuum annealing (18 h).<sup>[7]</sup> Thus, the observed distinct structural and property changes among the various implanted states offer further evidence of vacancy modulations in LSMO thin films using helium irradiation.

### 3. Conclusion

We have demonstrated a highly efficient means to induce ionic defects in epitaxial LSMO films at room temperature using helium implantation. By proper tuning of the implantation parameters, a transformation from ferromagnetic metal to antiferromagnetic insulator is achieved without destroying the film lattice or introducing any abrupt increase of roughness. In addition, the lattice strain of epitaxial thin films can be continuously manipulated along uniaxial direction by this approach, which offers a new playground for the optimization of nonvolatile memory, spintronics, and multifunctional devices.

### 4. Experimental Section

$\text{La}_{0.7}\text{Sr}_{0.3}\text{MnO}_{3-\delta}$  thin films were grown on (001)  $\text{SrTiO}_3$  substrates by HOPSD.<sup>[33]</sup> The samples were deposited at 800 °C with an oxygen partial pressure of 2 mbar. The vertical distance between the target and the substrate was fixed to 20 mm. Ion irradiation was performed near room temperature using a 200 kV ion implanter with 3.5 and 50 keV He ions to a fluence range of  $1 \times 10^{15}$ – $2.5 \times 10^{16} \text{ ions cm}^{-2}$ , with beam rastering to ensure uniform irradiation. Using the SRIM program, the projected range for the He ions, displacement per atom (DPA) and the vacancy profile are simulated.<sup>[34]</sup> The crystal structure and strain states were identified by XRD, XRR, and reciprocal space mapping measurements using a Panalytical X'pert four-circle X-ray diffractometer. Modeling of the reflectivity data was performed using the GenX software to determine film thickness as well as the roughness of the surface and interface.<sup>[35]</sup> The stoichiometry of LSMO films was determined using RBS. The measurements were performed with a collimated 1.7 MeV  $\text{He}^+$  beam of the Rossendorf van de Graff accelerator with a 10–20 nA beam current at a backscattering angle of 170°. Channeling geometry measurements were also collected by aligning the impinging  $\text{He}^+$  beam parallel to the STO



[001] axes. The magnetization of the films was measured by a superconducting quantum interference device equipped with a vibrating sample magnetometer (SQUID-VSM, Quantum Design). The magnetotransport measurements were conducted in a van-der-Pauw geometry using a Lake Shore Hall measurement system (resistance range: 40  $\mu\Omega$  to 200 G $\Omega$ ). In the resistivity measurement, the magnetic field was applied along the surface normal direction and perpendicular to the current direction.

## Acknowledgements

L.C. acknowledges financial support from the German Research Foundation (Grant No. ZH 225/10-1).

Open access funding enabled and organized by Projekt DEAL.

## Conflict of Interest

The authors declare no conflict of interest.

## Data Availability Statement

The data that support the findings of this study are available from the corresponding author upon reasonable request.

## Keywords

complex oxides, helium implantation, metal-to-insulator transition, oxygen vacancies, strain doping

Received: May 24, 2021

Revised: July 22, 2021

Published online: September 17, 2021

- [1] P. Yu, Y.-H. Chu, R. Ramesh, *Mater. Today* **2012**, 15, 320.
- [2] H. Yamada, *Science* **2004**, 305, 646.
- [3] R. Waser, R. Dittmann, G. Staikov, K. Szot, *Adv. Mater.* **2009**, 21, 2632.
- [4] S. V. Kalinin, N. A. Spaldin, *Science* **2013**, 341, 858.
- [5] N. Lu, P. Zhang, Q. Zhang, R. Qiao, Q. He, H.-B. Li, Y. Wang, J. Guo, D. Zhang, Z. Duan, Z. Li, M. Wang, S. Yang, M. Yan, E. Arenholz, S. Zhou, W. Yang, L. Gu, C.-W. Nan, J. Wu, Y. Tokura, P. Yu, *Nature* **2017**, 546, 124.
- [6] H. Jeon, W. S. Choi, M. D. Biegalski, C. M. Folkman, I.-C. Tung, D. D. Fong, J. W. Freeland, D. Shin, H. Ohta, M. F. Chisholm, H. N. Lee, *Nat. Mater.* **2013**, 12, 1057.
- [7] L. Cao, O. Petravic, P. Zakalek, A. Weber, U. Rücker, J. Schubert, A. Koutsoubas, S. Mattauch, T. Brückel, *Adv. Mater.* **2019**, 31, 1806183.
- [8] A. Khare, D. Shin, T. S. Yoo, M. Kim, T. D. Kang, J. Lee, S. Roh, I.-H. Jung, J. Hwang, S. W. Kim, T. W. Noh, H. Ohta, W. S. Choi, *Adv. Mater.* **2017**, 29, 1606566.
- [9] C.-H. Lee, N. D. Orloff, T. Birol, Y. Zhu, V. Goian, E. Rocas, R. Haislmaier, E. Vlahos, J. A. Mundy, L. F. Kourkoutis, Y. Nie, M. D. Biegalski, J. Zhang, M. Bernhagen, N. A. Benedek, Y. Kim, J. D. Brock, R. Uecker, X. X. Xi, V. Gopalan, D. Nuzhnyy, S. Kamba, D. A. Muller, I. Takeuchi, J. C. Booth, C. J. Fennie, D. G. Schlom, *Nature* **2013**, 502, 532.
- [10] D. Li, K. Lee, B. Y. Wang, M. Osada, S. Crossley, H. R. Lee, Y. Cui, Y. Hikita, H. Y. Hwang, *Nature* **2019**, 572, 624.
- [11] Y. Xie, M. D. Scafetta, R. J. Sichel-Tissot, E. J. Moon, R. C. Devlin, H. Wu, A. L. Krick, S. J. May, *Adv. Mater.* **2014**, 26, 1434.
- [12] H. Guo, S. Dong, P. Rack, J. Budai, C. Beekman, Z. Gai, W. Siemons, C. M. Gonzalez, R. Timilsina, A. T. Wong, A. Herklotz, P. C. Snijders, E. Dagotto, T. Z. Ward, *Phys. Rev. Lett.* **2015**, 114, 256801.
- [13] P. Pandey, Y. Bitla, M. Zschornak, M. Wang, C. Xu, J. Grenzer, D.-C. Meyer, Y.-Y. Chin, H.-J. Lin, C.-T. Chen, S. Gemming, M. Helm, Y.-H. Chu, S. Zhou, *APL Mater.* **2018**, 6, 066109.
- [14] H. Jeon, W. S. Choi, J. W. Freeland, H. Ohta, C. U. Jung, H. N. Lee, *Adv. Mater.* **2013**, 25, 3651.
- [15] Z. Li, S. Shen, Z. Tian, K. Hwangbo, M. Wang, Y. Wang, F. M. Bartram, L. He, Y. Lyu, Y. Dong, G. Wan, H. Li, N. Lu, J. Zang, H. Zhou, E. Arenholz, Q. He, L. Yang, W. Luo, P. Yu, *Nat. Commun.* **2020**, 11, 184.
- [16] J. D. Ferguson, Y. Kim, L. F. Kourkoutis, A. Vodnick, A. R. Woll, D. A. Muller, J. D. Brock, *Adv. Mater.* **2011**, 23, 1226.
- [17] J. Hemberger, A. Krimmel, T. Kurz, H.-A. Krug von Nidda, V. Y. Ivanov, A. A. Mukhin, A. M. Balbashov, A. Loidl, *Phys. Rev. B* **2002**, 66, 094410.
- [18] M. C. Martin, G. Shirane, *Phys. Rev. B* **1996**, 53, 285.
- [19] J.-S. Lee, D. A. Arena, P. Yu, C. S. Nelson, R. Fan, C. J. Kinane, S. Langridge, M. D. Russell, R. Ramesh, C.-C. Kao, *Phys. Rev. Lett.* **2010**, 105, 257204.
- [20] P. Yu, J.-S. Lee, S. Okamoto, M. D. Russell, M. Huijben, C.-H. Yang, Q. He, J. X. Zhang, S. Y. Yang, M. J. Lee, Q. M. Ramasse, R. Erni, Y.-H. Chu, D. A. Arena, C.-C. Kao, L. W. Martin, R. Ramesh, *Phys. Rev. Lett.* **2010**, 105, 027201.
- [21] D. Schumacher, A. Steffen, J. Voigt, J. Schubert, T. Brückel, H. Ambaye, V. Lauter, *Phys. Rev. B* **2013**, 88, 144427.
- [22] S. B. Adler, *J. Am. Ceram. Soc.* **2004**, 84, 2117.
- [23] S. Autier-Laurent, O. Plantevin, P. Lecoeur, B. Decamps, A. Gentils, C. Bachelet, O. Kaitasov, G. Baldinozzi, *Europhys. Lett.* **2010**, 92, 36005.
- [24] S. Leclerc, A. Declémy, M. F. Beaufort, C. Tromas, J. F. Barbot, *J. Appl. Phys.* **2005**, 98, 113506.
- [25] H. Palancher, P. Goudeau, A. Boule, F. Rieutord, V. Favre-Nicolin, N. Blanc, G. Martin, J. Fouet, C. Onofri, *Appl. Phys. Lett.* **2016**, 108, 031903.
- [26] S. Chen, H. Zhou, X. Ye, Z. Chen, J. Zhao, S. Das, C. Klewe, L. Zhang, E. Lupi, P. Shafer, E. Arenholz, D. Jin, H. Huang, Y. Lu, X. Li, M. Wu, S. Ke, H. Xu, X. Zeng, C. Huang, L. W. Martin, L. Chen, *Adv. Funct. Mater.* **2019**, 29, 1907072.
- [27] E. Dagotto, *Science* **2005**, 309, 257.
- [28] K. J. Choi, *Science* **2004**, 306, 1005.
- [29] S. Chen, C. Guan, S. Ke, X. Zeng, C. Huang, S. Hu, F. Yen, H. Huang, Y. Lu, L. Chen, *ACS Appl. Mater. Interfaces* **2018**, 10, 18029.
- [30] E. Dixon, J. Hadermann, M. A. Hayward, *Chem. Mater.* **2012**, 24, 1486.
- [31] P. Perna, C. Rodrigo, E. Jiménez, F. J. Teran, N. Mikuszeit, L. Méchin, J. Camarero, R. Miranda, *J. Appl. Phys.* **2011**, 110, 013919.
- [32] S. Kumari, N. Mottaghi, C.-Y. Huang, R. Trappen, G. Bhandari, S. Yousefi, G. Cabrera, M. S. Seehra, M. B. Holcomb, *Sci. Rep.* **2020**, 10, 3659.
- [33] U. Poppe, N. Klein, U. Dähne, H. Soltner, C. L. Jia, B. Kabius, K. Urban, A. Lubig, K. Schmidt, S. Hensen, S. Orbach, G. Müller, H. Piel, *J. Appl. Phys.* **1992**, 71, 5572.
- [34] J. F. Ziegler, M. D. Ziegler, J. P. Biersack, *Nucl. Instrum. Methods Phys. Res. Sect. B Beam Interact. Mater. Atoms* **2010**, 268, 1818.
- [35] M. Björck, G. Andersson, *J. Appl. Crystallogr.* **2007**, 40, 1174.